Geophysical Journal International

Geophys. J. Int. (2022) **228,** 927–943
Advance Access publication 2021 September 02
GJI Seismology

https://doi.org/10.1093/gji/ggab336

Modelling tilt noise caused by atmospheric processes at long periods for several horizontal seismometers at BFO—a reprise

W. Zürn [1], T. Forbriger [1,2], R. Widmer-Schnidrig [1,3], P. Duffner[1,4] and A.T. Ringler [5]

[1] *Black Forest Observatory (Schiltach), Karlsruhe Institute of Technology and University of Stuttgart, Heubach* 206, *D*-77709 *Wolfach, Germany. E-mail: thomas.forbriger@kit.edu*
[2] *Geophysical Institute (GPI), Karlsruhe Institute of Technology (KIT), Hertzstr.* 16, *D*-76187 *Karlsruhe, Germany*
[3] *Institute of Geodesy, University of Stuttgart, Geschwister-Scholl-Strasse* 24*D, D*-70174 *Stuttgart, Germany*
[4] *Geodetic Institute (GIK), Karlsruhe Institute of Technology (KIT), Englerstrasse* 7, *D*-76128 *Karlsruhe, Germany*
[5] *U. S. Geological Survey, Albuquerque Seismological Laboratory, PO Box* 82010, *Albuquerque, NM* 87198, *USA*

Accepted 2021 August 30. Received 2021 July 30; in original form 2021 March 30

SUMMARY

Tilting of the ground due to loading by the variable atmosphere is known to corrupt very long period horizontal seismic records (below 10 mHz) even at the quietest stations. At BFO (Black Forest Observatory, SW-Germany), the opportunity arose to study these disturbances on a variety of simultaneously operated state-of-the-art broad-band sensors. A series of time windows with clear atmospherically caused effects was selected and attempts were made to model these 'signals' in a deterministic way. This was done by simultaneously least-squares fitting the locally recorded barometric pressure and its Hilbert transform to the ground accelerations in a bandpass between 100 and 3600 s periods. Variance reductions of up to 97 per cent were obtained. We show our results by combining the 'specific pressure induced accelerations' for the two horizontal components of the same sensor as vectors on a horizontal plane, one for direct pressure and one for its Hilbert transform. It turned out that at BFO the direct pressure effects are large, strongly position dependent and largely independent of atmospheric events for instruments installed on piers, while three post-hole sensors are only slightly affected. The infamous 'cavity effects' are invoked to be responsible for these large effects on the pier sensors. On the other hand, in the majority of cases all sensors showed very similar magnitudes and directions for the vectors obtained for the regression with the Hilbert transform, but highly variable from event to event especially in direction. Therefore, this direction most certainly has to do with the gradient of the pressure field moving over the station which causes a larger scale deformation of the crust. The observations are very consistent with these two fundamental mechanisms of how fluctuations of atmospheric surface pressure causes tilt noise. The results provide a sound basis for further improvements of the models for these mechanisms. The methods used here can already help to reduce atmospherically induced noise in long-period horizontal seismic records.

Key words: Loading of the Earth; Transient deformation; Seismic instruments; Seismic noise; Site effects.

1 INTRODUCTION

1.1 Motivation and background

In studies of normal modes of the Earth based on long-period seismic records both for Earth structure and source mechanisms horizontal components are used much less frequently than vertical components. This is not a satisfactory situation. The major reason is probably the notoriously higher noise level at long periods in horizontal records even at very good stations (Berger *et al.* 2004). Most if not all of this unavoidable higher noise is caused by tilting of the ground by atmospheric loading (e.g. Beauduin *et al.* 1996, Wielandt 2002). This tilt couples a small projection of the gravity vector into the sensitive direction of the horizontal seismometer mimicking a competitive ground acceleration. Given enough information on the atmospheric pressure field as a function of space and time this coupling is a deterministic process; therefore deterministic descriptions of these induced signals could help to understand them.

Zürn *et al.* (2007) made an attempt to reduce long-period noise observed at the Black Forest Observatory (BFO, near Schiltach,

SW-Germany, 48.33°N, 8.33°E, 589 m amsl, for a description see Zürn 2014) in the frequency band of the normal modes of the Earth in broad-band horizontal seismograms with the help of the locally recorded atmospheric pressure. This was done by fitting the atmospheric pressure and its Hilbert transform simultaneously to the seismograms in a linear regression. Prior to these fits, the seismograms were converted to ground acceleration since we expected inertial and gravitational forces caused by atmospheric processes on the sensor mass to be responsible for the disturbances.

This method is motivated by a number of previous findings. First, as already stated above it is well understood and accepted in the seismological community that long-period horizontal noise is predominantly caused by tilt of the instrument due to the varying load of the atmosphere on the crust in the vicinity of a station (e.g. Sorrells 1971; Beauduin *et al.* 1996; Wielandt 2002; Berger *et al.* 2004). An inertial horizontal seismic sensor cannot distinguish in principle between translational horizontal acceleration and tilt of the ground (i.e. inertial acceleration versus tilt coupled gravity), thus it inevitably records both.

Secondly, Zürn *et al.* (2007) suggested two physical mechanisms which may cause local tilts and they were partially successful in reducing noise in the normal mode frequency band. The first mechanism consists of local elastic deformation of the environment of the seismometer and/or station due to the changing atmospheric load. The resulting deformation field is strongly influenced by the local boundary conditions such as the geometry of the cavity and fissures, the topography and the geology. This contribution is equivalent to the infamous local elastic effects (often called 'cavity effects' even when it is not clear whether the cavity geometry is responsible or other very local heterogeneities) disturbing the measurement of tilt and strain tides of the solid Earth and rendering interpretation of such measurements in terms of Love numbers essentially impossible (e.g. Baker & Lennon 1973; King & Bilham 1973; Harrison 1976; for BFO, see Emter & Zürn, 1985 and Lambotte *et al.* 2006). King *et al.* (1976) predicted that eventually these effects will show up in seismograms, which was demonstrated by Zürn *et al.* (2007), Park *et al.* (2008) and Ringler *et al.* (2019). Since this effect is due to the linear elastic response of the structures it should somehow be proportional to the local atmospheric pressure. Zürn *et al.* (2007) called this the local deformation tilt (LDT). In the LDT model, we treat the air-pressure variation to be laterally homogeneous (which it rarely will be) but it is really only the pressure variation above the station and its immediate neighbourhood which is responsible for the deformation. The coefficient describing this effect should be independent of the amplitude and waveform of the pressure variation. Therefore for a given seismometer component one single number should describe the response to the whole spectrum of driving loads. However, these numbers can vary very much from place to place within one observatory. In addition the induced signals should be in phase with pressure but the sign may flip, that is, the waveform of the observed tilt should be identical to the waveform of the pressure variation except possibly for polarity. There may also be locations within an observatory where the LDT-effect vanishes in one or both components. Actually we demonstrate below that this is nearly the case for the post-hole seismometers at BFO. Predictions of the LDT coefficients for different locations within the BFO-mine using finite-element (FE) models can be found in the contributions by Steffen (2005), Steffen *et al.* (2006), Zürn *et al.* (2007, their table 2) and Gebauer *et al.* (2010).

The second effect is theoretically caused by a horizontally travelling harmonic plane pressure wave. Another, simpler, concept would be an only temporally varying horizontal gradient of air pressure. Möckli (1988) found at a station near Zürich, Switzerland, that the waveform of long-period disturbances in horizontal broad-band seismograms resembled the Hilbert transform of the locally recorded barometric pressure. Based on the work by Sorrells (1971), Zürn *et al.* (2007) developed a theoretical model (called TWT, i.e. travelling wave tilt) showing that such a wave causes tilts which are proportional to the Hilbert transform of the local atmospheric pressure. The Hilbert transform of a signal has a phase shift of 90° for each frequency present in the signal, that is, it is orthogonal to the original signal (LDT). For that mechanism all parallel oriented seismometer components installed sufficiently close to each other should have the same coefficient for the TWT (in contrast to LDT) since they all experience the same tilt in response to the pressure variation. However, this mechanism can only work alone, if the LDT-coefficient is zero for a particular seismometer. If this is not the case TWT cannot occur without LDT at the same time. LDT possibly may be at work alone, if the atmosphere stays horizontally layered and changes occur only in vertical direction, which is probably rarely the case.

The full description of the TWT-mechanism as derived by Zürn *et al.* (2007, their eq. 13) and based on the work by Sorrells (1971) contains two additional terms besides the frequency independent tilt effect. The first term is the gravitational attraction which is only mildly dependent on frequency. The other term is the inertial acceleration due to purely horizontal motion and this is strongly dependent on frequency (Zürn *et al.* 2007, eq. 13, fig. 8). All three effects are in quadrature to local atmospheric pressure. However, at the frequencies in the band considered here the tilt effect by far dominates the other two for reasonable values of the elastic moduli and therefore only the tilt effect was used to describe the TWT-model in Zürn *et al.* (2007) and in this work.

Clearly both models are simplifications of the processes happening in the atmosphere and of the acting coupling mechanisms and may be compared with the famous proverbial 'spherical cow'. Nevertheless, they are models which are physically reasonable. However, one has to keep in mind that the parameters obtained by fitting the TWT-model to accelerograms are necessarily highly variable in time because, for example, different atmospheric phenomena may closely follow each other and disturbances travel in different directions with different velocities and wavelengths, anyway, so that the projection of the resulting tilt onto the sensitive axis of the horizontal seismometer varies. For the LDT-model the parameters have to be expected to be highly variable in space due to local heterogeneities near the surface, as is demonstrated for BFO by Steffen *et al.* (2006), Zürn *et al.* (2007), Gebauer *et al.* (2010) and the current paper.

Thirdly, Alejandro *et al.* (2020) looked at air pressure effects in the data from several stations of the Global Seismographic Network (GSN) in the United States (ANMO, CCM, HRV, TUC and WCI) with a wide spectrum of installation conditions and seismometers. At all these places two individual broad-band seismometers are being operated. These authors used the models described in the previous paragraphs (without mentioning the physics behind these models) and investigated the directions into which instruments tilt when air pressure rises. They also checked the coherence between horizontal seismograms and local air pressure and in their Fig. 13 presented plots of the LDT versus TWT coefficients as we do below in a different form in Figs 10 and 11. In contrast to their work, we identify similar behaviour caused by air-pressure variations at several places within the mine for the TWT-model.

1.2 Instruments and their installation

In the work by Zürn *et al.* (2007) horizontal seismograms from three stations installed within BFO were examined. The authors did not look specifically at simultaneously recorded data from these three installations. The instruments examined were the station of the German Regional Seismic Network (GRSN), equipped with the STS-2, the station belonging to the network of the Incorporated Research Institutions for Seismology/International Deployment of Accelerometers (IRIS/IDA), equipped with three STS-1s (Wielandt & Streckeisen 1982), and a prototype station belonging to E. Wielandt at ETH, Zürich (three prototype STS-1s, called STS-0s by Zürn *et al.* 2007). Figs 1 and 2 show maps of the locations described in the following. The former two stations were installed on concrete piers attached to the South-wall (S-wall) of the BFO seismometer vault, the latter on a concrete pier attached to the North-wall (N-wall) of the same vault (see Figs 1 and 2). The authors presented cases of atmospheric disturbances where the two simultaneously used models LDT and TWT resulted in variance reductions of 90 per cent, in other cases the efficiency was much lower (maybe down to 20 per cent) and almost did not justify the effort. It turned out that the NS-components reacted strongly to the LDT, while the TWT did show up clearly on the EW-components, a specific behaviour at BFO. By the way, the method was also successfully applied to records of the BFO strainmeters after the megaquakes off the NW-coast of Sumatra in 2004 and the Tohoku event in 2011 (Zürn *et al.* 2015).

The current contribution goes beyond the study by Zürn *et al.* (2007) in that more instruments in different setups could be used and that the examples we show were recorded simultaneously, which is essential when TWT-coefficients are compared as will become clear below. We focus mostly on cases where the models appear appropriate and the variance reductions are significant, but we also include a few cases which show anomalous behaviour.

In the last couple of years tests of different broadband seismometers were performed at BFO and the opportunity arose to look at properties of other installations in addition to the STS-1s of the IDA/IRIS network and the STS-2 of the GRSN used by Zürn *et al.* (2007). The STS-1/NS seismometer was moved to the northern pier in the seismic vault early in 2017, while the STS-1/EW and the STS-2 remained where they were in 2007. The STS-0 was removed completely when the STS-1-station was first installed in 1994.

A Nanometrics Trillium T360 triaxial seismometer (serial number SN 0052) shielded by a black plastic dome was temporarily installed on the same pier where the STS-1/EW seismometer was installed since 1994.

In late-2019 three Streckeisen 3-component STS-6As were installed in three shallow boreholes in the *N*300°*E*-strainmeter tunnel (Figs 1 and 2c). In this study, the only instruments installed in post-holes are the STS-6As. This tunnel also houses one of the BFO invar wire strainmeters (Zürn *et al.* 2015) and one arm of the long baseline differential pressure fluid tiltmeter runs along it as well (Ferreira *et al.* 2006). The boreholes were drilled through a new concrete pier sitting directly on the granite. The post-holes are about 0.5 m apart along the 'symmetry axis' of the tunnel and each is 1.60 m deep. It was conjectured that in the symmetry axis of a tunnel the tilts due to LDT should be minimized [this idea was first proposed by Harrison (1976) from his finite element (FE) computations and verified at BFO for the tidal strains (Emter & Zürn 1985) using ASKANIA borehole tiltmeters]. Stainless steel pipes were inserted into the holes and the seismometers installed in those. The exterior and interior of the steel pipes were not filled with grout or concrete but with amber blast, a chemically inert, fine grained (0.1–1.0 mm) hard sandlike material. Seen from the centre of the strainmeter array the sequence of the individual seismometers is SN176254, SN176241 and SN150804 (for short these are called STS65, STS64 and STS60, respectively, in the diagram legends using the digit before the last in the serial number). For a description of these instruments and their installation, see also Forbriger *et al.* (2021) and Table 1.

In a few time windows accelerograms from five additional instruments were analysed in parallel to the sensors above: (1) the ASKANIA borehole tiltmeter SN10, modified earlier (Zürn *et al.* 2000) and now freshly mounted on the eastern wall of the *N*2°*E*-strainmeter tunnel. The mounting is as described in fig. 3 of Emter & Zürn (1985) and sketched in fig. 2d. (2) An additional STS-1/NS seismometer was installed temporarily on the northern pier of the seismic vault. (3) Two STS-2s (SN99112 and SN99113) were installed on the big concrete pier in the so-called 'Heinrich'-Cleft and recorded on a Centaur (SN115) and a Quanterra Q330HR digitizer (SN4409). In short, we refer to these sensors by S112 and S113, respectively. The big tidal cavity effects in this cleft are described in Emter & Zürn (1985). The S112 was sitting in the back on a gabbro-slab, wrapped in wool and covered with the stainless steel cooking pot used in the GRSN (Forbriger 2012, fig. 3) which is again wrapped in wool and covered with a space blanket. The S113 is only wrapped in wool and covered by a space blanket and it is sitting in front to the NW of the other one.

All seismometers are triaxial Galperin-type sensors within one single casing, except the STS-1 for which each component is a separate unit.

The barometer is a Paroscientific MET4-device mounted high up on the outside wall of the laboratory building at its northern end. The barometer located in the magnetics hut and indicated also in Fig. 1 is the same type and shows nearly identical signals in the normal mode band as the one used in this work. Since the used barometer is located at a distance of about 480 m from the farthest seismometers systematic errors arise in our analyses due to propagation of the atmospheric pressure fields. However, from the results of several tests not reported here we conclude that they are not larger than the uncertainties caused by other systematic and random errors. The time delays between the two pressure signals were found to be not larger than 16 s and the contribution of the Hilbert transform of one to the other did not exceed 5 per cent.

2 METHODS

Prior to analysis the seismic data were corrected for instrumental response to obtain ground acceleration in units of nm s^{-2}. Positive values indicate acceleration of the ground and the frame of the instrument in up-, N- and E-directions, respectively. The accelerograms were filtered with a fourth-order Butterworth low-pass filter with an eigenfrequency of 10 mHz and subsequently a second-order Butterworth highpass filter with eigenfrequency of 1/3600 Hz was applied twice. The barometer record was filtered with the same filters. The resulting bandpass is designed for the low-frequency normal modes. The units are nm s^{-2} and hPa for the accelerograms and barograms and their Hilbert transforms, respectively.

Time windows with energetic atmospheric events in this frequency band and with no earthquakes or obvious gliches in the data

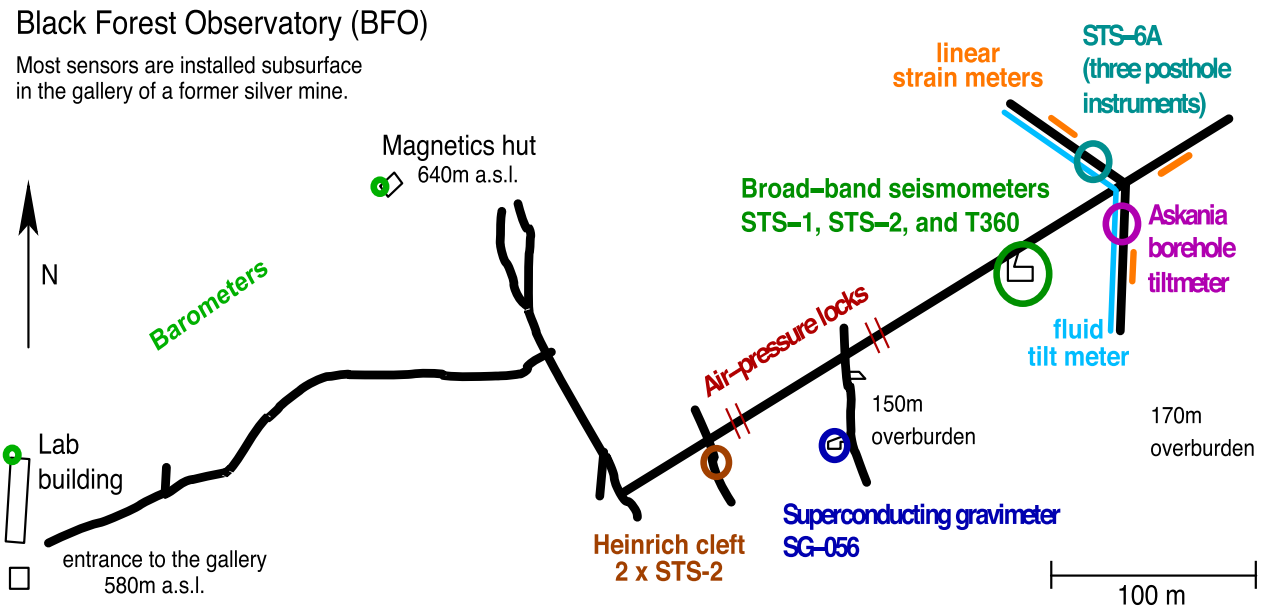

Figure 1. Map of the BFO (48.33°N, 8.33°E). The seismic instruments are installed in a former silver/cobalt mine dug into granite. The main tunnel rises by about 10 m from the adit to the crossing tunnel. The first air lock separates the sensors from the outside and the second one separates additionally the seismo-, tilt- and strainmeters from the superconducting gravimeter with its cooling system. Overburden increases steeply along the main tunnel and is 150–170 m for the part behind both air locks. The barometer used in the work here is located at the northern end of the laboratory building.

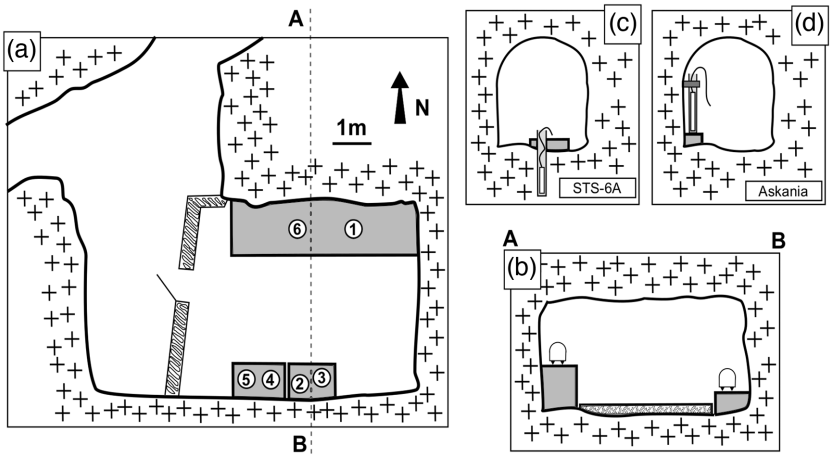

Figure 2. (a) Floor plan and (b) NS-cross-section A–B of the seismic vault at BFO. Positions of seismometers are indicated as follows: (1): STS-1/NS (IRIS/IDA), (2): STS-1/EW, (3): Trillium T-360, (4): STS-2, (5): STS-1/Z and (6): STS-1/NS (#2). (c) Cross-section across one of the post-hole installations and (d) of the Askania pendulum installation at the eastern wall of the tunnel. Shaded grey indicates concrete piers. Scale in left-hand panel is approximately valid for all sketches.

were selected and the available data retained from as many seismometers as possible. We concentrated first on the NS-components because in our daily routine monitor plots it was observed that many large pressure effects of these components for the STS-1 and the STS-2 consisted in tilts in opposite directions, a fact observed already by Zürn *et al.* (2007) for the STS-0/NS on one hand and the STS-1/NS and STS-2/NS on the other hand. The STS-1/NS was then still installed on the southern pier and showed the same polarity as the STS-2/NS. This was always understood as an effect of the floor of the vault (the cavity) bulging due to the pressure load and thus tilting in opposite directions near the S- and N-walls where the piers are located (bulging of the walls was clearly observed with several tiltmeters in the pendulum vault (now housing the SG-056, Fig. 1) of BFO as a reaction to the mostly horizontal straining by the Earth tides, for example, Emter & Zürn (1985). However, a closer inspection of the reactions of the two NS-seismometer components sometimes showed phase shifts different from 180° and we decided to take another look at this phenomenon and in addition look at other seismometers in the BFO mine as listed above. These observations lead to a higher number of analyses for NS- than for EW-components. Table 2 presents information on the time windows, the seismometers and the components analysed.

For the selected time windows the Hilbert transform $HT(t)$ of the barometric pressure outside the mine was computed. The seismic sensors with the exception of the S112 and S113 are located behind two efficient air locks which act as a low-pass filter for the air pressure with a time constant of 40–60 h (this time constant is

Table 1. Instruments used in this study are identified by sensor type and serial number. The data source (Black Forest Observatory 1971) is specified by the SEED network code(Net), station code (Station), location code (Loc) and channel code (Channels). The last column shows the IDs of these sensors used in the paper. Metadata can be obtained from the IRIS MetaData Aggregator (**ds.iris.edu/mda/**) based on these SEED codes. Station code XBFO (experimental) is used for temporary installations.

Sensor	Serial-Nr	Net	Station	Loc	Channels	ID
STS-1	18784		BFO		LHN	STS1-N
STS-1	18783	II	BFO	00	LHE	STS1-E
STS-2	19123	GR	BFO		LHN, LHE	STS2
STS-2	99112		BFO		LHN, LHE	S112
STS-2	99113		BFO		LHN, LHE	S113
STS-1	16	II	BFO	00	LHN	STS1-N #2
STS-6A	150804	II	XBFO	55	LHN, LHE	STS-6A0
STS-6A	176241	II	XBFO	60	LHN, LHE	STS-6A4
STS-6A	176254	II	XBFO	50	LHN, LHE	STS-6A5
T360	0052	II	XBFO	70	LHN, LHE	T360
ASKANIA	BLP 10				LHN, LHE	ASK
Parosci-6016B	90720	II	BFO	10	LDO	Pa
Parosci-MET4	106787		BFO			Pa
SG-056-G1	056	II	BFO	00	LG1	G1
SG-056-G2	056	II	BFO	00	LG2	G2

Table 2. Dates, number of windows used for these dates, components and seismometers used in the attempts to reduce the noise caused by atmospheric processes. The sensors are described in the main text and listed in Table 1. The number given is the highest variance reduction (per cent) obtained for the sensor in any window on these days. '–' indicates that this seismometer could not be used for that day. The remarks in the rightmost column identify additional sensors included in the analyses for the respective dates together with the variance reduction obtained for them.

Date	Windows	Components	STS-1	STS-2	T360	STS-6A-0	STS-6A-4	STS-6A-5	Remarks
04/03/2017	1	N,E	90	94	–	–	–	–	
01/03/2018	3	N	79	77	–	–	–	–	
11/03/2018	4	N	97	97	–	–	–	–	
15/03/2018	2	N	96	93	–	–	–	–	
01/06/2018	1	N,E	84	83	–	–	–	–	ASK 52 per cent
20/10/2019	1	N	88	91	–	–	–	–	
15/11/2019	1	N,E	87	86	84	74	–	–	
16/11/2019	3	N,E	89	89	85	78	–	–	
17/11/2019	1	N,E	89	92	90	78	–	–	STS1/N #2 79 per cent
25/02/2020	3	N	54	74	72	17	19	27	
26/02/2020	1	N	38	47	44	9	10	15	
27/02/2020	1	N	9	22	23	10	10	12	
29/02/2020	2	N,E	57	53	53	63	65	67	
01/03/2020	1	N,E	61	55	52	57	54	49	
02/03/2020	1	N,E	89	88	84	85	85	84	
07/03/2020	1	N	39	55	35	2	31	35	STS1/N #2 9 per cent
11/05/2020	5	N,E	93	95	94	95	95	96	S112 93 per cent, S113 94 per cent
22/05/2020	4	N,E	93	94	95	93	93	93	
23/05/2020	5	N,E	84	87	84	83	83	85	
03/08/2020	1	N,E	93	87	–	86	87	88	
25/09/2020	1	N,E	93	89	–	76	77	77	
05/11/2020	1	N,E	63	66	–	46	50	46	
15/11/2020	1	N,E	78	78	–	83	83	84	

slightly variable because on occasion people move through the lock thereby slightly modifying the tightness of the seals). Then the method of least squares was used to fit the recorded pressure $p_a(t)$ and its Hilbert transform $HT(t)$ to the different accelerograms $s(t)$ resulting in two coefficients for each accelerogram with the units nm s^{-2} hPa^{-1} and residuals $r(t)$ with (hopefully) tilt signals caused by the atmospheric phenomena removed from (or reduced in) the data. The superscript s refers to the accelerogram under analysis emphasizing that the coefficients are expected to be different for each sensor and component.

$$s(t) = c_p^s \cdot p_a(t) + c_{HT}^s \cdot HT(t) + r(t)$$

The efficiency of the method is estimated by calculating the variance reduction R defined by $R = (\sigma_0^2 - \sigma_1^2)/\sigma_0^2$ and given as percentage. σ_0^2 is the variance of the accelerogram $s(t)$ and σ_1^2 the variance of the residual time-series $r(t)$. The highest R obtained on each day for the best component of each sensor and the best window can be found in Table 2.

A nice feature of this model function is that $p_a(t)$ and $HT(t)$ are orthogonal functions, that is, their cross-correlation at lag zero vanishes, and in practice the values become negligibly small when finite window lengths are considered. This orthogonality was checked by least-squares fitting of $HT(t)$ to $p_a(t)$, which resulted always in extremely small coefficients. Fig. 3 shows a bandpassed pressure record and its Hilbert transform for the time window from 14:00 to 16:00 UTC on 2020 May 22 as an example (this example is discussed in more detail in Section 4.3). Figs 4 and 5 depict NS-accelerograms from the STS-1 and STS-2, respectively, for the time window 10:30 to 13:30 UTC on 2020 March 2 together with the bandpassed pressure and its Hilbert transform for visual comparison. The similarity of the waveforms is striking, however, the different phase shifts between accelerogram, pressure and Hilbert transform are conspicuous and can only be understood by a combination of the two tilt mechanisms LDT and TWT.

We show four examples demonstrating pressure effects and their reduction for six seismometers. The first example in Fig. 6 is for NS-components in the time window 10:00 to 14:00 UTC on 2020 March 2 (see Section 4.2), the second (Fig. 7) for EW-components from 10:00 to 22:00 UTC on 2020 February 29, the third (Fig. 8) for NS-components from 11:00 to 15:00 UTC on 2020 May 11 and the fourth (Fig. 9) for the EW-components of the same window (see Section 4.1). On the left, the bandpassed accelerations are shown together with the barometric pressure (multiplied by a factor of 30 $\mathrm{nm\,s^{-2}\,hPa^{-1}}$ for better comparison). On the right, the residuals after fitting pressure and its Hilbert transform are depicted. Significant reduction of the long-period pressure-correlated disturbances is obvious.

However, it is also obvious that for higher frequencies our 'correction' does not work as well as for the long-period disturbances (Fig. 7, right-hand panel). In Fig. 8, one can even see that with the 'correction' higher frequency oscillations at about 2.5 mHz present in the pressure record but not large in the records from the post-hole seismometers appear in the residuals for the NS-components of these, in other words the 'correction' injects the 2.5 mHz signals into the residuals.. The same oscillations are observed in the original EW-accelerograms of the same time window (Fig. 9) at about equal amplitude in the post-hole and pier records and are slightly reduced in the residuals of both.

3 SUMMARY OF RESULTS FOR TIME WINDOWS OF TABLE 2

In Figs 10 (NS-components) and 11 (EW-components), the results of the fits for all the windows in Table 2 are depicted by plotting the coefficient c^s_{HT} for the HT and seismometer component s versus the corresponding coefficient c^s_p. Later on the acronyms LDT and TWT are used for c^s_p and c^s_{HT}, respectively (although this is already a kind of interpretation).

We recall that the same method for noise reduction with only the direct pressure as model function is used routinely for records from gravimeters, much less for data from vertical seismometers (Zürn & Widmer 1995; Zürn & Wielandt 2007; Forbriger *et al.* 2021). To our knowledge only Zürn & Timmen (2018) have so far used the Hilbert transform in the model for vertical components. For the vertical components, the coefficient c^s_p mostly results in values around about $-3.5\,\mathrm{nm\,s^{-2}\,hPa^{-1}}$. The $HT(t)$ is normally not used because it usually does not contribute significantly (however, see Section 4.5) and a physical motivation does not exist to our knowledge. Such values for c^s_p are found consistently at many stations around the world, notably Jackson & Slichter (1974) reported a value of $-0.48\ \mu\mathrm{Gal\,(mm\ Hg)^{-1}}$ ($-3.6\ \mathrm{nm\,s^{-2}\,hPa^{-1}}$) from the geographic South Pole. The effect in the vertical components is well understood to be predominantly caused by varying Newtonian attraction of the sensor mass by the atmosphere with varying air density and much less by deformation of the crust, while in horizontal components, the tilt by deformation dominates other contributions (Zürn *et al.* 2007).

The first observation is that at BFO the factors c^s_p obtained for all horizontal components that are installed on piers, but especially in the NS-direction are up to 10 times larger than is usual for vertical components. This is certainly one of the reasons why long-period horizontal noise is larger by such factors than the long-period vertical noise (Berger *et al.* 2004, fig. 7). Müller & Zürn (1983) already pointed this out in data from one of the first ever modern broad-band seismometer sets (STS-0 at BFO, STS-1 prototypes installed by E. Wielandt at BFO). In contrast the LDT-coefficients for the post-hole NS-instruments have the order of magnitude usually observed for vertical accelerometers or even smaller.

The second observation is the clustering of the LDT-coefficients for the NS-components. There are three groups: large negative values for the sensors sitting on the northern pier of the seismic vault (STS-1/NS, STS-1/NS #2), small and mostly positive values for the borehole sensors (three STS-6As), and larger positive values for the sensors sitting on the southern piers of the seismic vault (STS-2, T-360). This spread for the pier instruments is consistent with the results by Zürn *et al.* (2007). The scatter for the EW-components is appreciable, albeit in a smaller numerical range than for NS-components, and no clustering is detectable. The coefficients for the post-hole installations tend to be somewhat smaller for LDT.

The difference in sign of the LDT-coefficients for the NS-components on the northern and southern piers in the BFO seismic vault can be explained by the deformation (bulging) of the floor causing tilts in opposite directions at opposite sides of the vault. If $c^s_p > 0$, the tilt is to the S for $\delta p_a > 0$, the floor and ceiling of the vault both bulge inward, and the floor tilt near the N-wall (S-wall) must be to the N (S), respectively. This is known in earth tidal research as a 'local elastic effect', or short 'cavity effect' (under this label often and here as well any local heterogeneity in structure or boundary conditions is understood). Of course, the stress situation for tides is quite different from the one for atmospheric loading. If only this process would be occurring then no phase shifts other than 0° or 180° should be observed. Furthermore all results for one sensor should collapse into one point in diagrams of c^s_p vs. c^s_{HT} (e.g. Figs 10 and 11) on the horizontal axis, and the TWT-coefficients should vanish. Not to forget, of course, the results are affected by noise from other sources, for example seismic surface waves from small earthquakes, the Earth's continuous background free oscillations (Kurrle & Widmer-Schnidrig 2006, 2008), and possibly magnetic field variations (Forbriger 2007, Forbriger *et al.* 2010). However, the observed phase shifts differing from 0° or 180° triggered this revisit of the problem, together with the larger number of simultaneously operating instruments available.

The processes LDT and TWT (and others), of course are active simultaneously. Therefore, the symbols in Figs 10 and 11 scatter appreciably and the phase shift between the northern and southern

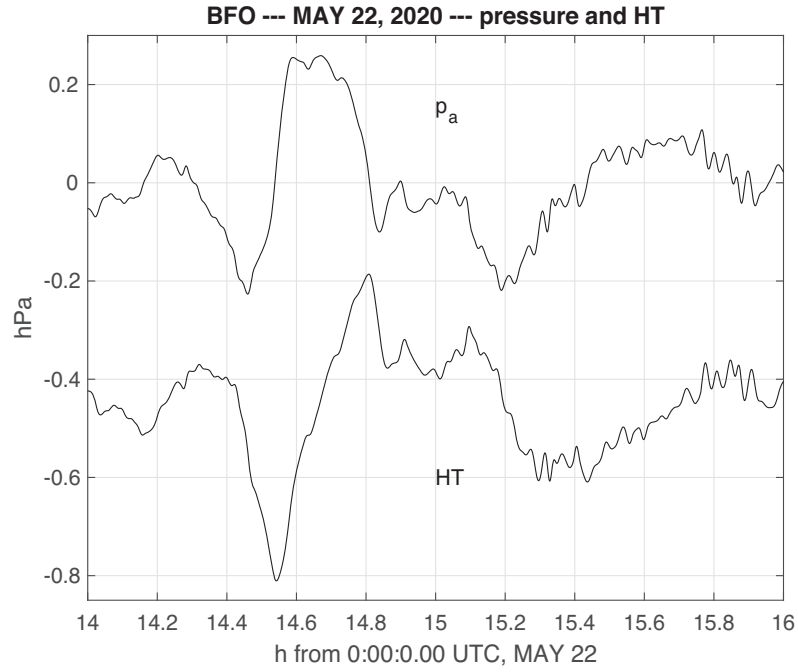

Figure 3. Pressure signal and the corresponding Hilbert transform for the time window defined in the title and horizontal axis. The Hilbert transform is offset by −0.5 hPa for clarity.

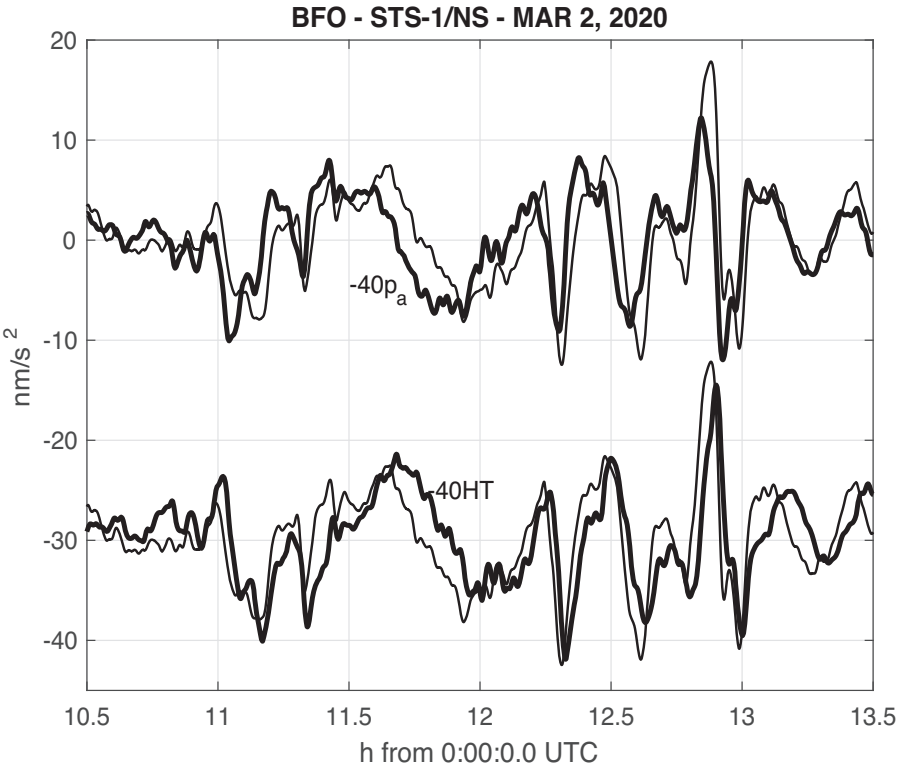

Figure 4. Pressure signal (top, thick line) and the corresponding Hilbert transform (bottom, thick line, offset by -30 nm s^{-2}) separately compared to the same STS-1 NS-accelerogram (thin line) for the time window 10:30 to 13:30 on 2020 March 2. The two pressure signals have been multiplied by -40 nm s^{-2} hPa^{-1}.

piers can easily deviate from 180°. Depending on the direction in which the atmospheric wave travels or in other words, in which direction the gradient of the pressure field is pointing, the magnitude and the signs of the TWT-coefficients vary appreciably, of course. However, the LDT-effect is extremely strong for the NS-components on the piers.

The third observation is that no such clear pattern emerges for the EW-components. For a single event tilting the crust in the direction

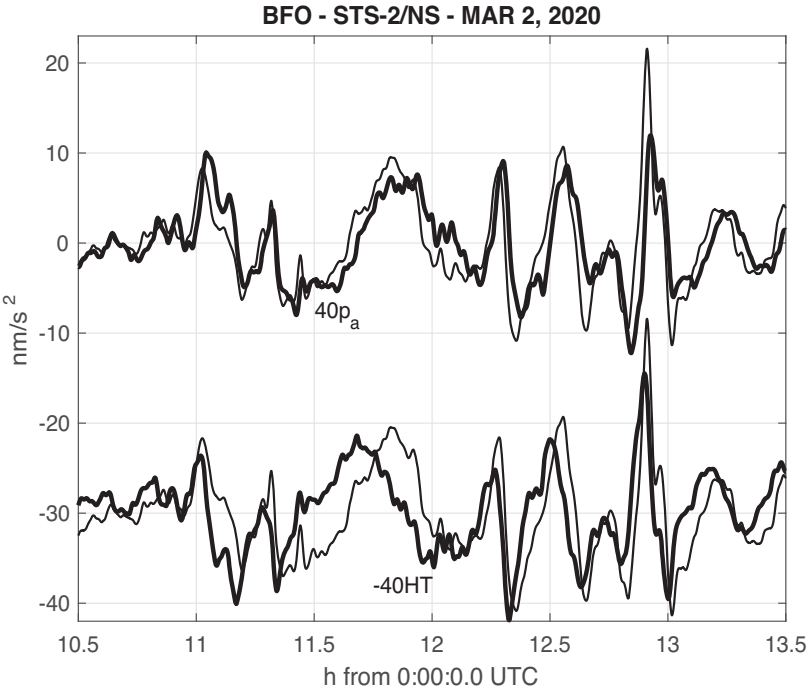

Figure 5. Same as Fig. 4, but for the STS-2 NS-accelerogram. However, in the upper trace the pressure was multiplied by $+40\ \mathrm{nm\,s^{-2}\,hPa^{-1}}$ and the Hilbert transform in the lower trace by $-40\ \mathrm{nm\,s^{-2}\,hPa^{-1}}$.

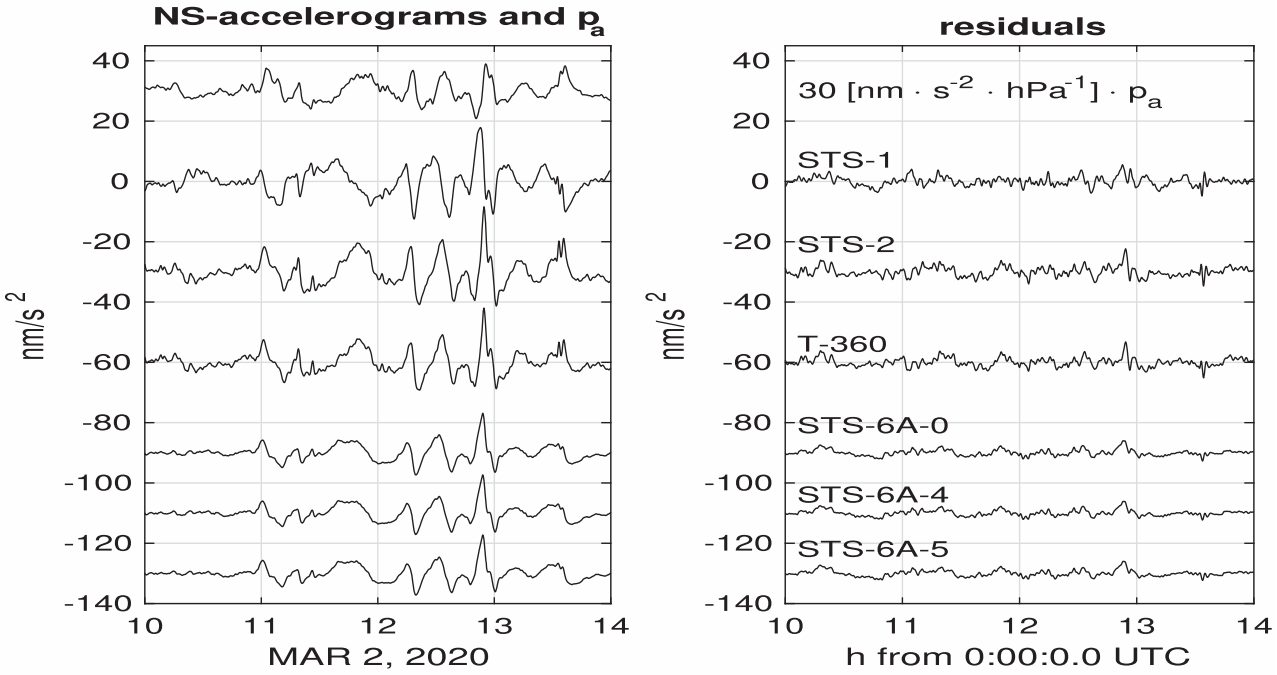

Figure 6. Left-hand panel: bandpassed NS-accelerograms for six broad-band seismometers in the time window from 10:00 to 14:00 UTC on 2020 March 2, and bandpassed atmospheric pressure (top trace). The pressure was multiplied by a factor of $30\ \mathrm{nm\,s^{-2}\,hPa^{-1}}$ for a better comparison with the effects in the accelerograms, as indicated at the top of the right-hand panel. Right-hand panel: residual accelerograms after least-squares fitting and subtracting of $p(t)$ and $HT(t)$. The individual sensors are identified next to the traces. The uppermost trace in the left-hand panel is identified at the top of the right-hand panel. Different offsets for the traces are introduced for better comparison.

of the pressure gradient the TWT-coefficients should be identical for all seismometers, only differing between NS- and EW-components, of course, and differing from event to event. In the case of the TWT, the whole area is supposed to tilt in a certain direction by the same amount; therefore all sensors should respond similarly. However, when LDT-coefficients are not small, this will not be the case, since different LDT-coefficients for the different sensors will introduce scatter.

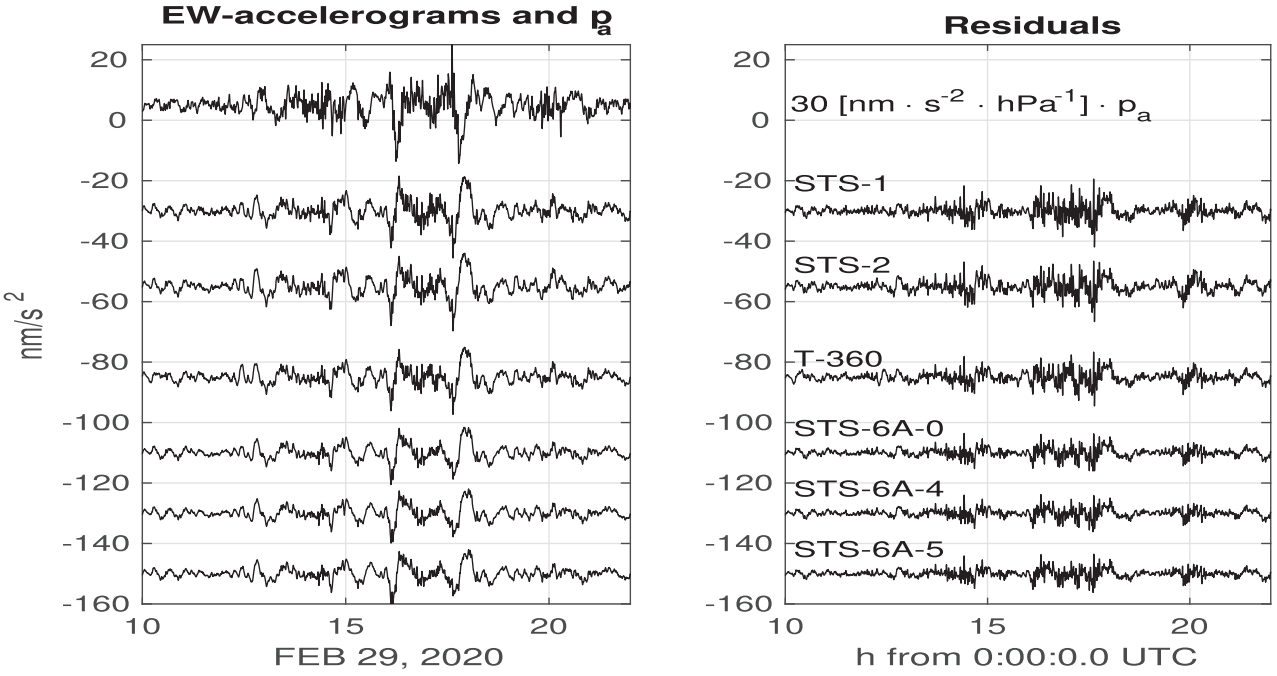

Figure 7. Same as Fig. 6, but for EW-components and the time window from 10:00 to 22:00 UTC on 2020 February 29. Note that the higher frequency noise conspicuous in the residuals (right-hand panel) is also present in the barogram. The uppermost trace in the left-hand panel is the scaled barogram with the scale factor given at the top of the right-hand panel.

4 SPECIAL EVENTS

Horizontal accelerations and tilts of the ground can be described as 2-D vectors in a horizontal plane while pressure and its Hilbert transform are scalars. In this section, we show the coefficients for individual pressure events also as vectors in a horizontal plane (or map, Figs 12–17). These could be called 'specific pressure acceleration vectors', at least in the case of c_p^s. The vectors point into the direction into which the ground appears to be accelerated due to the increasing atmospheric pressure load $p_a(t)$ or the increasing Hilbert transform $HT(t)$, respectively. The plots on the left-hand sides show the coefficients c_p^s as vectors with components in NS- and EW-directions, on the right-hand sides the coefficients c_{HT}^s are depicted in the same manner. The units are $\mathrm{nm\,s^{-2}\,hPa^{-1}}$. The coefficients c_p^s can be converted to corresponding tilt coefficients (in $\mathrm{nrad\,hPa^{-1}}$) in the opposite direction by multiplying the values by $-g^{-1}$, where $g = 9.81\ \mathrm{m\,s^{-2}}$ is local gravitational acceleration. For the Hilbert transform, we can understand the vectors as indicating the vertical plane in which the tilt takes place irrespective of the sign of the actual tilt. The relation of this tilt to the gradient of the pressure field cannot be clarified because the HT does not carry any directional information since it is computed from a locally recorded scalar time series. For example, local elastic effects (topography and geology) could have an influence again and modify the loading effect such that the azimuthal angle of the tilt deviates from the direction of the gradient and that the magnitude of the tilt depends on the direction too (a kind of anisotropy).

Recall that inertial sensors, as used here exclusively, cannot distinguish in principle between purely horizontal acceleration and tilt. The tilt direction is the direction into which the bob of a vertical pendulum moves (this is a definition, of course).

4.1 2020 May 11

On this day, a cold front moved through the region of BFO causing relatively rapid pressure fluctuations. Accelerograms from six seismometers are shown for the NS- and EW-components in Figs 8 and 9, respectively. In each case, the local atmospheric pressure multiplied by $30\ \mathrm{nm\,s^{-2}\,hPa^{-1}}$ is also shown for easy visual comparison of waveforms. The data are processed as described above. The results for the time window between 11:00 and 15:00 UTC are shown. The left-hand panels show the data and the right-hand panels the residuals $r(t)$ after subtracting the model functions. The reduction of the very long period disturbances is impressive and the variance reductions are of the order of 95 per cent.

However, note the 'high-frequency' oscillations in pressure and in all EW- and three NS- accelerograms starting shortly before 13:00 and lasting for about 40 min. Their dominant frequency is 2.5 mHz. Obviously the coefficients found to reduce the much bigger very long period variations do not handle these oscillations well (i.e. the necessary coefficients for those are different from the ones for the big variations). These 2.5 mHz-oscillations are even enhanced in the data from the STS-6A-NS seismometers (lowest three traces in the right-hand panel in Fig. 8) because they are injected by the subtraction of the model function to form the residuals. For reasons like this the term 'barometric correction' should always be understood with a 'grain of salt'.

In Fig. 12, we plot the obtained coefficients as vectors in a horizontal plane. The spread of the obtained LDT-coefficients is very large for NS-data. However, the TWT-coefficients for each component are nearly identical (EW) or very close to each other (NS). So this result is almost exactly the one expected for a TWT. Clearly, a cold front is a travelling disturbance with a pressure gradient. The obtained variance reductions are in each case averaged for the

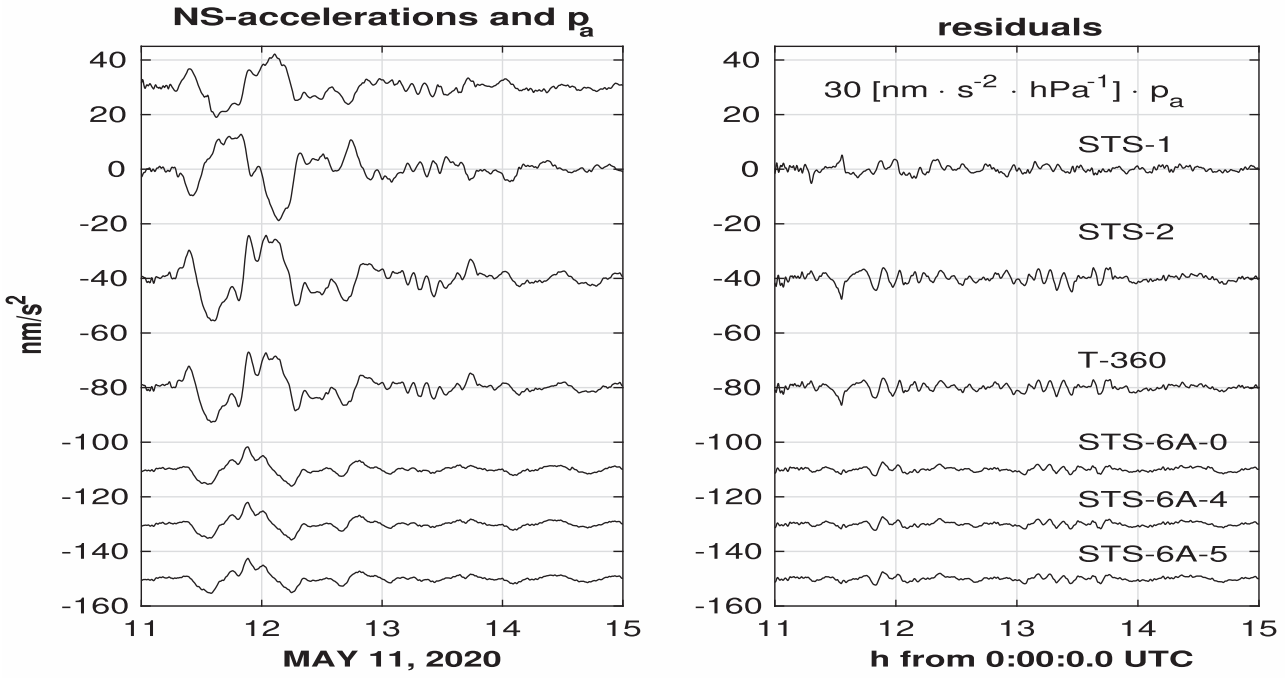

Figure 8. Left-hand panel: bandpassed NS-accelerograms for six broadband seismometers in the time window from 11:00 to 15:00 UTC on 2020 May 11, and bandpassed atmospheric pressure (top trace). The pressure was multiplied by a factor of 30 $\mathrm{nm\,s^{-2}\,hPa^{-1}}$ for a better comparison with the effects in the accelerograms as indicated at the top of the right-hand panel. Right-hand panel: residual accelerograms after the least-squares fitting of $p(t)$ and $HT(t)$. The individual sensors are identified next to the traces. Note the short-period oscillations (2.5 mHz) in the pressure after 13:00 UTC, which also appear in some of the accelerograms. The uppermost trace in the left-hand panel is identified at the top of the right-hand panel.

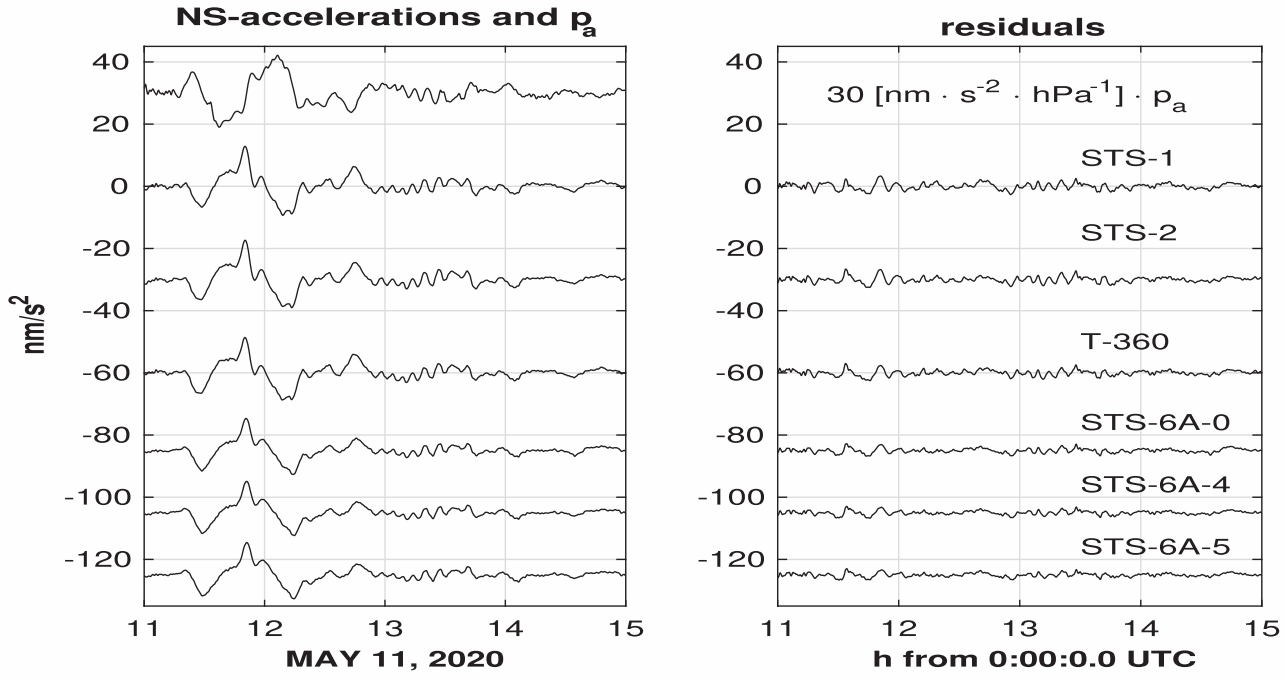

Figure 9. Same as Fig. 8, but for EW-components and the same time window.

six seismometers, separately for each component: NS: 87.2 per cent and EW: 91.4 per cent. The left-hand panel therefore shows, in which direction a certain sensor tilts when the pressure on top of the station decreases. In case of the STS-1, this is not quite true, since the NS-component is located on a different pier than the EW-component, but it can be called an apparent tilt of the STS-1 station as a whole. Thus, the STS-1-station apparently tilts to the NNE when pressure increases, the STS-2 and the T-360 to the SSE, and the three STS-6As tilt much less in S to SE direction. The right-hand panel shows that all six seismometers tilt in response to the TWT signal by similar amounts in very similar directions, in this case NE–SW.

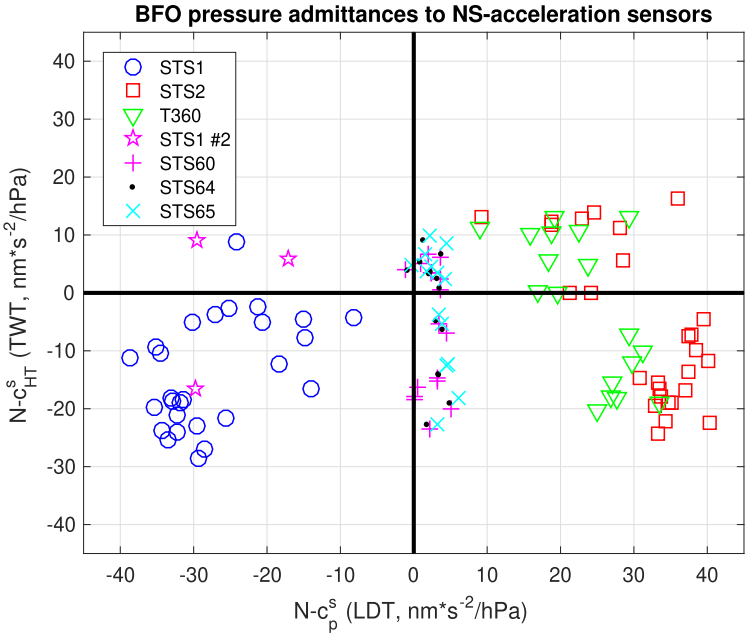

Figure 10. TWT-coefficients c^s_{HT} versus LDT-coefficients c^s_p for all the time windows examined for NS-components. The symbols are described in the legend. 'STS1 #2' is the second STS-1/NS temporarily installed on the northern pier in the seismic vault.

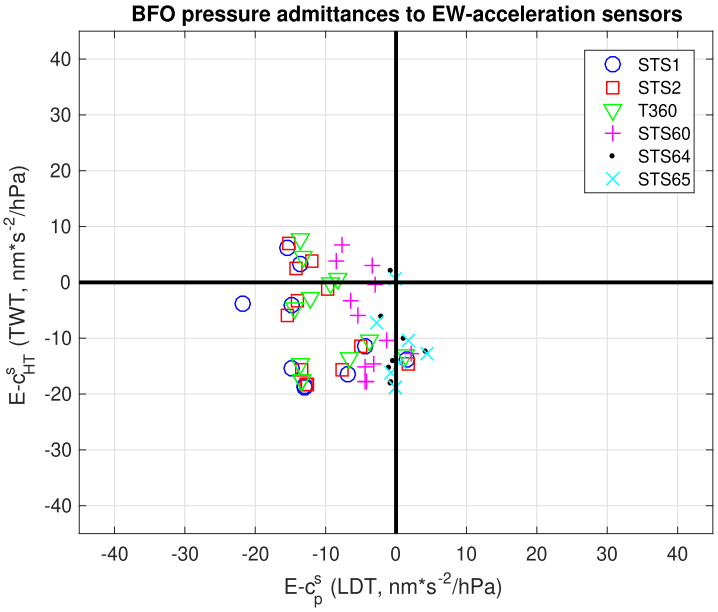

Figure 11. TWT-coefficients c^s_{HT} versus LDT-coefficients c^s_p for all the time windows examined for EW-components. The symbols are described in the legend. Less windows were used for EW than for NS for reasons explained in the text. The range of the axes in this diagram are intentionally the same as in Fig. 10.

For this time window we also examined the reaction of the two STS-2 seismometers on the pier in the 'Heinrich'-cleft. Recall that these two units, S112 and S113, are not behind the airlocks. Ambient pressure there is equivalent to outside pressure in contrast to the parts of the mine behind the airlocks, therefore a direct influence of p_a on the seismometers (such as deformation of the case) or on the pier (such as elastic deformation due to asymmetric boundary conditions) cannot be ruled out for these two sensors. Fig. 13 shows the results for these two sensors together with the ones for the STS-2 in the seismic vault (GR, already shown in Fig. 12). The two seismometers in the 'Heinrich'-cleft are sitting on the same concrete block and still respond to the LDT into different directions which indicates either a direct pressure effect on at least one of them or some deformation of the pier or a combination of both.

Local deformations in the 'Heinrich'-cleft have been investigated previously. A 1 m invar-bar strainmeter across this cleft showed apparent strains for Earth tides and seismic waves which were amplified by a factor of approximately 50 with respect to the strains along the tunnel in the same azimuth (Emter & Zürn 1985). In the case of the atmospheric effects, which we study here, the load on this cavity is quite different from the essentially horizontal tidal stresses. In addition one must consider that the pressure load also acts on the

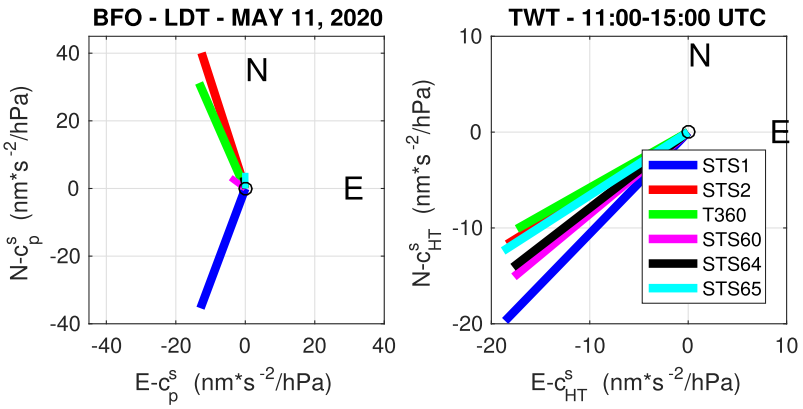

Figure 12. Plots of the NS- and EW-results for each sensor as vectors in a horizontal plane. Window 11:00 to 15:00 UTC on 2020 May 11. Left-hand panel: LDT-coefficients c^s_p. Right-hand panel: TWT-coefficients c^s_{HT}. Sensors are identified in the legend. Note that in the left-hand panel the STS64 arrow is nearly covered by the one for STS65.

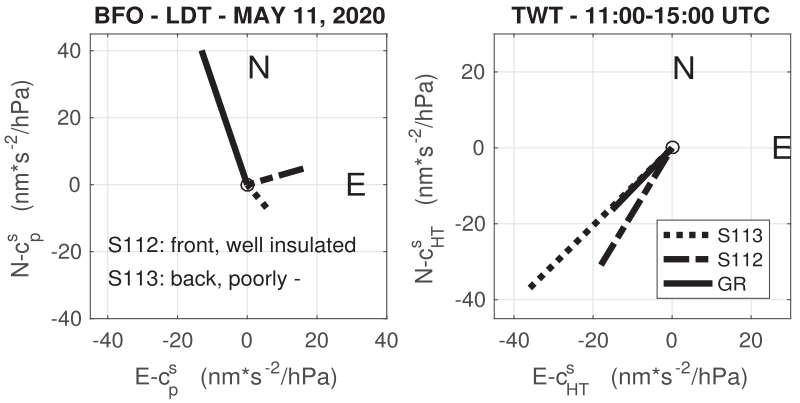

Figure 13. Plots of the NS- and EW-results for three STS-2s as vectors in a horizontal plane. Window 11:00 to 15:00 UTC on 2020 May 11. Left-hand panel: LDT-coefficients c^s_p. Right-hand panel: TWT-coefficients c^s_{HT}. Sensors are identified in the legend.

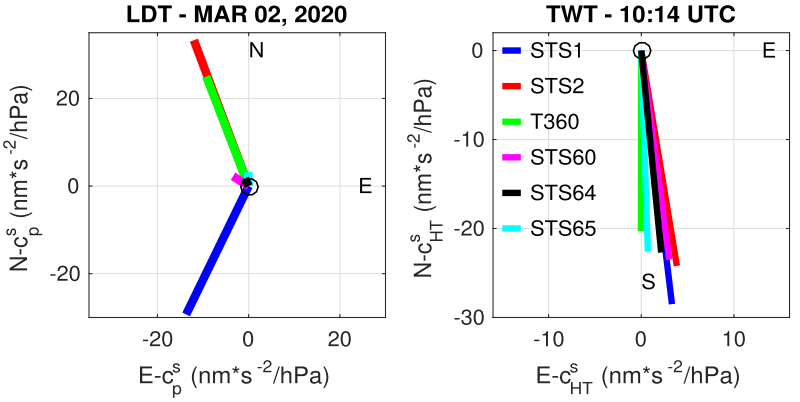

Figure 14. Plots of the NS- and EW-results for six seismometers as vectors in a horizontal plane. Window 10:00 to 14:00 UTC on 2020 March 2. Left-hand panel: LDT-coefficients c^s_p. Right-hand panel: TWT-coefficients c^s_{HT}. Sensors are identified in the right-hand panel.

walls of the cleft from inside (and on the seismometers directly). Therefore, the apparent high amplification of the deformation by the tides cannot be expected as well for the deformation induced by the atmospheric pressure. The pressure loading the inside walls of the cleft must be expected to make deformations smaller. The comparison with the STS-2 of the GR shows that this appears to be the case. The directions of the tilts out-of-phase with the local pressure (TWT-coefficients, Fig. 13, right) again show behaviour somewhat (but not quite) consistent with the STS-2 (GR) behind the two airlocks.

4.2 2020 March 2

From 2020 February 29 to March 2 several pressure disturbances with energy in the normal mode frequency band moved through the area of BFO. Several of these were analysed as described. Fig. 6 shows data and post-fit residuals for the NS-components of six seismometers between 10:00 and 14:00 UTC on March 2 together with the amplified pressure signal. The results derived for all these windows are depicted in Figs 10 and 11. Fig. 14 shows the coefficients plotted as vectors on a horizontal plane. For the

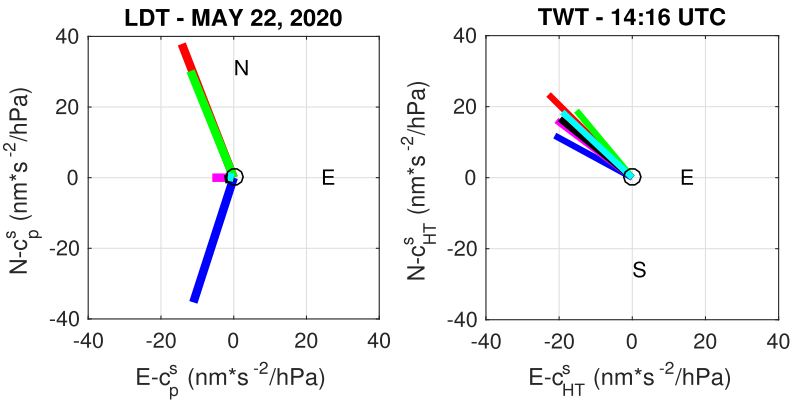

Figure 15. Plots of the NS- and EW-results for six seismometers as vectors in a horizontal plane. Window 14:00 to 16:00 UTC on 2020 May 22. Left-hand panel: LDT-coefficients c_p^s. Right-hand panel: TWT-coefficients c_{HT}^s. Sensors are identified in the legend of Fig. 14.

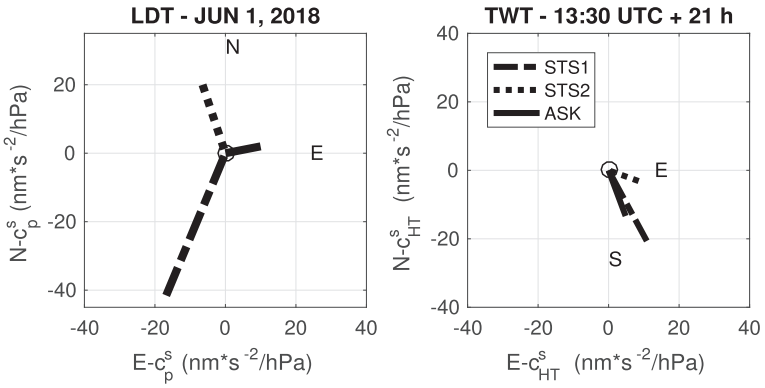

Figure 16. Plots of the NS- and EW-results for three accelerometers as vectors in a horizontal plane. Window starting at 13:30 UTC on 2018 June 1 and 21 hr long. Left-hand panel: LDT-coefficients c_p^s. Right-hand panel: TWT-coefficients c_{HT}^s. Sensors are identified in the legend.

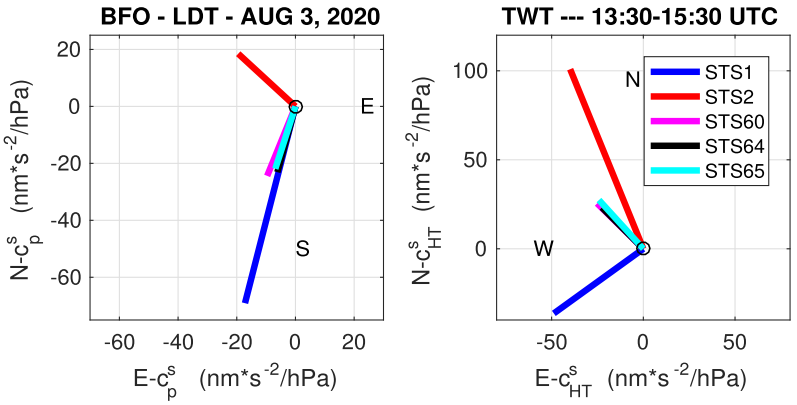

Figure 17. Plots of the NS- and EW-results for five seismometers as vectors in a horizontal plane. Window from 13:30 UTC until 15:30 on 2020 August 3. Left-hand panel: LDT-coefficients c_p^s. Right-hand panel: TWT-coefficients c_{HT}^s. Sensors are identified in the legend.

NS-components, the LDT-coefficients are spread out as before, while the TWT-coefficients are very close to each other. In EW, the spread for LDT is much smaller and the TWTs cluster very nicely about one small positive value.

The directions and magnitudes of the c_p^s coefficient vectors are very different again for the LDT. Pier instruments show large values and the STS-1 tilts the other way of the STS-2 and T-360 (northern vs. southern piers in the seismic vault), while all the STS-6As in the post-holes show very small values. The TWT-tilts of all six sensors are very big and very close in direction to each other. It appears that the pressure field was rigidly tilting the entire BFO mine almost directly in north–south direction.

4.3 2020 May 22

The two days 2020 May 22 and 23 offered many pressure disturbances and several windows were selected for analyses. The results for these are included in Figs 10 and 11, but here we present information for the window from 14:00 to 16:00 UTC on May 22 only.

Table 3. Pressure admittances obtained for the signal which occurred on 2020 August 3, between 13:30 and 15:30 at BFO. The admittances of pressure to gravity are also listed because of their very unusual values. The last column shows the variance reductions obtained.

Sensor	Component	c_p^s	c_{HT}^s	Variance reduction
–	–	nm s^{-2} hPa^{-1}	nm s^{-2} hPa^{-1}	per cent
STS-1	NS	– 69.1	– 36.3	86.9
STS-2	NS	18.5	100.9	79.9
STS-6A-0	NS	– 24.4	25.5	75.6
STS-6A-4	NS	– 23.1	23.2	76.5
STS-6A-5	NS	– 21.9	27.4	76.5
STS-1	EW	– 17.2	– 48.8	74.0
STS-2	EW	– 19.5	– 39.9	73.2
STS-6A-0	EW	– 9.6	– 25.2	65.9
STS-6A-4	EW	– 6.2	– 22.6	61.9
STS-6A-5	EW	– 6.9	– 24.2	64.3
SG-056-G1	Z	– 5.5	– 7.0	87.1
SG-056-G2	Z	– 5.6	– 7.3	83.1

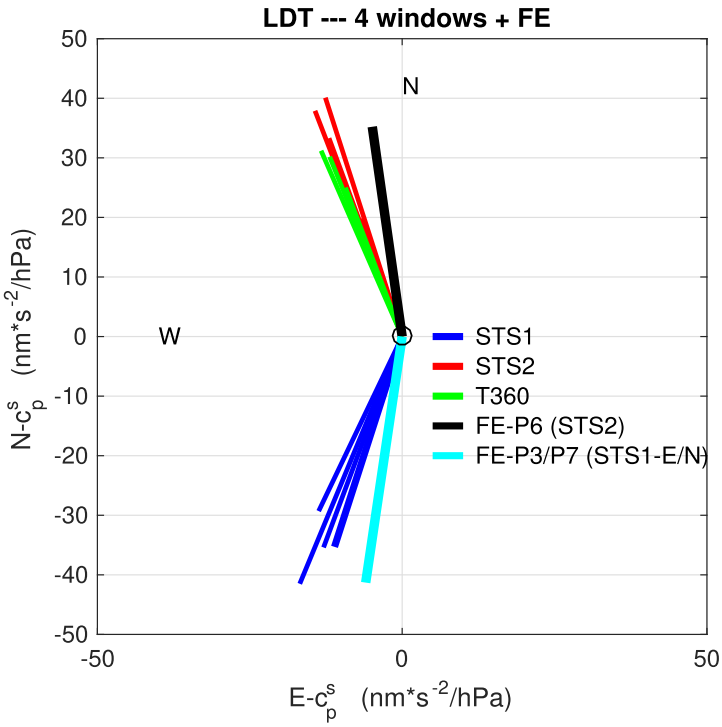

Figure 18. Plot of the c_p^s- coefficients (LDT) as vectors in a horizontal plane for the piers in the seismic vault of BFO. The observations for three seismometers were obtained in four windows as detailed in Section 4.6 (STS-1, STS-2 and T-360). The results for the FE model are from Gebauer *et al.* (2010): FE-P6 (STS2) for the position of the STS-2 on the southern pier and FE-P3/P7 (STS1-E/N) for the positions of the STS-1/EW on the southern and the STS-1/NS on the northern pier, respectively.

This window contains an especially nice pressure pulse in the normal mode frequency range which is shown in Fig. 3 together with its Hilbert transform. The average variance reductions obtained in this window are 89.3 per cent for the NS- and 91.0 per cent for the EW-components. Fig. 15 shows the coefficients as vectors in a horizontal plane and the behaviour is similar to what is observed in the previously analysed windows (note the consistency of the responses to LDT in Figs 12, 14 and 15, which must be expected for this mechanism). For the NS-components, the LDT-coefficients are big and spread out between ±40 nm s^{-2} hPa^{-1} with the polarity inversion between northern and southern piers and the post-hole sensors showing very small effects. The TWT-coefficients are closer to each other and positive with the post-hole sensors very similar to the others at about 18 nm s^{-2} hPa^{-1}. For the EW-components, the spread is much smaller for LDT than for the NS-sensors and basically there is very little spread for the TWT-coefficient.

4.4 2018 June 1

A thunderstorm passed over the BFO on this day associated with big pressure variations in the normal mode frequency band. We show the results as vectors in a horizontal plane in Fig. 16. There are only three accelerometers used: STS-1, STS-2 and the Askania-BLP10. Clearly the broad-band seismometers behave as usual with the exception that for the TWT-coefficient vectors the difference in direction is larger than usual between the two STS-seismometers.

The Askania tiltmeter shows a larger effect for the LDT than is typical for the STS-6As, but smaller than all pier instruments. This is basically a borehole instrument but at BFO it is sitting on the floor at the wall on a little concrete pier and mounted with a flange to the wall of the N2°E—tunnel on its eastern side (see Fig. 2d). This type of installation in the vault where the superconducting gravimeter is now located lead to huge tidal cavity effects due to bulging of the N- and S-walls of that room (Emter & Zürn 1985). At the S-wall, the cavity effect tilt for diurnal tides had the opposite sign of the body tide. The body tide tilt for diurnal tides in NS-direction is rather small at the latitude of BFO and since the cavity effect tilt was large it even overwhelmed the body and ocean load tide tilts to give a phase of 180° with respect to the predicted body tide. This effect was essentially predicted by Harrison (1976). For the Askania-tiltmeter at its present position and under the pressure load on the surface the EW-component (essentially perpendicular to the wall) was expected to react more strongly than it did in the case here. However, the direction of the vector for c_p^s (LDT) is towards the E, indicating that this instrument tilts to the W when the pressure above BFO increases and that the tunnel wall is bulging inward.

4.5 2020 August 3

A coldfront-like disturbance passed through the region on this day. The pressure change in the normal mode band did not exceed 0.4 hPa peak-to-peak, but it had a good signal-to-noise ratio, therefore it was analysed, and it turned out to be an unusual event as far as the magnitude of the resulting coefficients are concerned. These are, for the window from 13:30 to 15:30 UTC, depicted as vectors in a horizontal plane in Fig. 17 and given in Table 3. In this table, the coefficients are listed in detail for their sheer magnitude as compared to other events. The LDT-coefficients show the usual directions of the coefficient vectors albeit with much larger magnitudes, here also for the post-hole instruments. The directions for the TWT-values agree for the post-hole instruments very nicely, but the pier instruments show completely different directions with huge magnitudes. The maximal, minimal and mean variance reduction R obtained for the NS-components were 86.9, 75.6 and 79.1 per cent, for the EW-components 74.0, 61.9 and 67.9 per cent, respectively. On the side we mention that in the time window from 13:58 to 14:14 UTC the rain gauge at BFO measured 11.2 $\mathrm{l\,m^{-2}}$ of cumulative rain. We speculate that the atmospheric phenomenon causing all this was quite unusual. Events like this are one of the reasons why we consider to install a barometer array around BFO.

The fact that this event was a special case is corroborated by an analysis of the gravity signals. The results for all the seismometer Z-components are very similar. In Table 3, we list in addition to the results for the horizontal components the corresponding results for the two spheres of the double-sphere superconducting gravimeter GWR-SG-056 (G1 is the 4 times heavier lower sphere providing better signal-to-noise ratios, e.g. Rosat & Hinderer 2011). c_p^s is almost twice as large as the usual value of about $-3.5\ \mathrm{nm\,s^{-2}\,hPa^{-1}}$ obtained for gravimeters essentially everywhere on the globe. The c_{HT}^s, which is normally not used in a fit to gravity (and when it is used it is normally negligible) turns out even larger. The non-orthogonality of the p_a and $HT(t)$ was especially checked for this case by least-squares fitting $HT(t)$ to p_a and found to be negligible.

This event is really less understood than all the others and is therefore included here while the corresponding coefficients c_p^s and c_{HT}^s for the horizontal components are not included in Figs 10 and 11. It again demonstrates that the term 'barometric correction' should be used with care. Any additional information on the pressure field could allow a better understanding of such cases.

4.6 Comparison of LDT-coefficients with finite-element models

Steffen *et al.* (2006) provided coefficients c_p^s for BFO using refined 3-D FE models of the mine and its vaults. The outer air lock was simulated by exluding air pressure loads on all the walls behind the first two doors. The results for several versions of this model are listed by Zürn *et al.* (2007, table 2), however, only the refined model with the air lock closed is relevant to the work here. Later Gebauer *et al.* (2010) refined the model further and in Fig. 18 we plot their results for the N- and S-piers in the seismic vault together with some results obtained here for the seismometers on these piers. The STS-1/NS were sitting on the N-pier, the STS-1/EW, the STS-2 and the T360 were sitting on the S-piers. Therefore Gebauer *et al.*'s (2010) results for their position P6 was used to simulate the reaction of the STS-2 (and possibly the T-360) and their positions P3 and P7 to simulate the responses of the STS-1/NS and STS-1/EW, respectively. The components of the vectors for the STS-1 are not connected physically to each other, since the two horizontal sensors are sitting on two different piers at opposite walls of the seismic vault (Fig. 2, right).

The results of our analyses for the following windows already discussed above and presented in Figs 12 and Section 4.1 (2020 May 11, 11:00 to 15:00 UTC), Fig. 14 and Section 4.2 (2020 Mar 02, 10:00 to 14:00 UTC), Fig. 15 and Section 4.3 (2020 May 22, 14:00 to 16:00 UTC), and Fig. 16 and Section 4.4 (2018 June 01, 13:30 to Jun 02, 10:30 UTC), are presented in Fig. 18 together with the FE results of Gebauer *et al.* (2010). T-360 was not available in 2018.

The directions of the observed LDT-vectors coincide almost with the FE results and the magnitudes of the modelled effects are really close. For the models by Steffen *et al.* (2006), the directions also corresponded well with the observed ones but the magnitudes were factors of 0.5 and 0.3 smaller than the magnitudes obtained by Gebauer *et al.* (2010) for the N- and S-piers, respectively.

One cannot expect that even a very detailed FE model is able to capture all the details affecting the elastic response. Especially every feature (cracks, small cavities, elastically weak zones, etc.) behind the walls is unknown. Taking this into account the correspondence of model predictions and observations must be considered very good.

5 DISCUSSION AND CONCLUSIONS

When temporal fluctuations of atmospheric pressure are large in the normal mode frequency range we observed that the waveforms of horizontal accelerations recorded with nine different broad-band sensors at BFO show high similarity either to the waveform of the air pressure record $p_a(t)$ or its Hilbert transform $HT(t)$ (the latter also representing a version of the air pressure but phase-shifted by $\pi/2$ at all frequencies), or a linear combination of both. Tilts caused by atmospheric loading are well known for being a major source of long-period seismic noise.

As proposed by Zürn *et al.* (2007), we model the expected signals by fitting $p_a(t)$ and $HT(t)$ to the observations whereby coefficients c_p^s and c_{HT}^s are determined using least squares. We interpret the contributions to the signals as 'local deformation tilt' (LDT) and 'travelling wave tilt' (TWT), respectively. With nine sensors we are

able to demonstrate that these models go a long way to describe the observations.

We find that in most cases the c_p^s-coefficients for NS-components are not as much dependent on the event but very much on the position of the sensor inside the mine. We found the range of these coefficients to be between ± 40 nm s^{-2} hPa^{-1}. The large negative values occur for the STS-1/NS on the northern pier in the seismic vault, the big positive values were found for the STS-2/NS and T-360/N on the pier on the southern side. Very small values were obtained for the three post-hole sensors (STS-6A/NS), mostly positive and below about 7 nm s^{-2} hPa^{-1}. Some of the latter are even negligible within the uncertainties. For the c_p^s for EW-components the range of values was much smaller, between -23 and $+$ 5 nm s^{-2} hPa^{-1}. Again the values for the post-hole sensors were smaller in magnitude than for the pier sensors, with the largest magnitude coefficient being -8 nm s^{-2} hPa^{-1}, and some of them are not distinguishable from zero. The NS-coefficients c_p^s show a clear pattern with three very distinct clusters, while the EW-coefficients c_p^s are much more scattered and no clear clusters occur.

The picture is quite different for the TWT c_{HT}^s-coefficients. Here, the values for both components vary strongly from event to event, but essentially all sensors have similar coefficients, differing for components, for a given event. The ranges here are from -30 to $+20$ nm s^{-2} hPa^{-1} for the NS-components and between -20 and $+8$ nm s^{-2} hPa^{-1} for the EW-components.

We feel that we do understand the LDT-effect physically rather well. The comparison of many of our observed c_p^s-coefficients with the results from a detailed FE model of the topography, the cavities, and the piers shows that this interpretation is probably correct. The large c_p^s for the NS-components result from the upward bulging of the floor of the seismic vault with the piers tilting perpendicular to the corresponding wall when pressure increases.

The TWT-effects result in tilts which somehow are little affected by the direct properties of an instrument site (e.g. vault geometry). Since the coefficient vectors are nearly independent of the sensor but vary strongly from event to event they have to do with the moving pressure field.

However, in Section 4.5, we present an example which falls very clearly out of the general pattern described above. Reasons for this large deviation are unknown at present and show again our limitations in the knowledge of the pressure field in time and space having only a local record of atmospheric pressure. The first step in that direction would be the operation of a small scale (order of aperture 1–2 km) barometer network around BFO.

Clearly, the fact that at BFO NS-sensors on piers react very strongly to p_a (LDT) is caused by the special arrangement of the piers inside the mine. This is certainly different at the majority of other stations. For the TWT-model all sensors should react, and mostly they do, in exactly the same way to the $HT(t)$ for a given event.

Since we are dealing with very small 'signals' here, we must keep in mind other contributions to the seismograms: seismic wave 'noise', magnetic field effects, possible thermal convection effects inside the vault, and always possible instrumental glitches not conspicuous enough to be detected by inspection of the (filtered) time-series.

We suggest that a better understanding of the pressure field around the station could help to better understand the phenomenon of tilt noise. A time stepping numerical model of the atmosphere with assimilation of data from a barometer network might improve the quality of the assumed forcing, which is still very simple in the work presented here. In all the studied cases, the LDT-mechanism produces smaller disturbances for post-hole sensors than for pier instruments and this presents a significant improvement. In the long run, we hope to be able to develop a pressure correction methodology that further improves long-period horizontal component signal-to-noise ratios. This will be necessary for stations where this cannot be achieved by emplacement techniques (type of installation, such as post-holes), which can only mitigate the LDT-type contributions.

6 DATA AND RESOURCES

The instruments used in this investigation are listed in Table 1. Data for GSN stations in this paper are available from the IRIS Data Management Center (DMC) under network code II (Scripps Institution of Oceanography 1986). The facilities of Incorporated Research Institutions for Seismology (IRIS) Data Services, and specifically the IRIS Data Management Center (DMC), were used for access to waveforms, related metadata and/or derived products used for this study. IRIS Data Services are funded through the Seismological Facilities for the Advancement of Geoscience and EarthScope (SAGE) Proposal of the National Science Foundation under Cooperative Agreement EAR-1 261 681. Any use of trade, product, or firm names is for descriptive purposes only and does not imply endorsement by the U. S. Government.

ACKNOWLEDGEMENTS

We thank Robert Freudenmann (Streckeisen GmbH, Pfungen, Switzerland), Steffen Uhlmann (Ingenieurgesellschaft für Geophysikalische Messtechnik (IGM), for Nanometrics), Sarvesh Upadyahya (Nanometrics Inc., Ottawa, Canada), Erhard Wielandt and Ludger Timmen (Inst. f. Erdmessung, Leibniz-University, Hannover, Germany) for loaning instruments used in this work. David Kyle Jones (ASL) helped to drill the post-holes for the STS-6As. Holger Steffen and André Gebauer performed FE simulations under the supervision of Thomas Jahr at the University of Jena. We also thank Erhard Wielandt for many very fruitful discussions and two anonymous reviewers, Rob Anthony, Brian Shiro, and Janet Slate for many helpful comments on the manuscript.

REFERENCES

Alejandro, A.C.B., Ringler, A.T., Wilson, D.C., Anthony, R.E. & Moore, R.V., 2020. Towards understanding relationships between atmospheric pressure variations and long-period horizontal seismic data: a case study, *Geophys. J. Int.,* **223,** 676–691.

Baker, T.F. & Lennon, G.W., 1973. Tidal tilt anomalies, *Nature,* **243,** 75–76.

Beauduin, R., Lognonné, P., Montagner, J.-P., Cacho, S., Karczewski, J.F. & Morand, M., 1996. The effects of atmospheric pressure changes on seismic signals or how to improve the quality of a station, *Bull. seism. Soc. Am.,* **86,** 1760–1769.

Berger, J., Davis, P. & Ekström, G., 2004. Ambient earth noise: a survey of the global seismographic network, *J. geophys. Res.,* **109,** B11307, doi: 10.1029/2004JB003408.

Black Forest Observatory (BFO), 1971. Black Forest Observatory Data, doi:10.5880/BFO.

Emter, D. & Zürn, W., 1985. Observations of local elastic effects on Earth tide tilts and strains, In: *Earth Tides, Benchmark Papers in Geology Series,* pp. 309–327, ed. Harrison, J.C., Van Nostrand Reinhold, New York.

Ferreira, A.M.G., d'Oreye, N.F., Woodhouse, J.H. & Zürn, W., 2006. Comparison of fluid tiltmeter data with long period seismograms: surface waves and Earth's free oscillations, *J. geophys. Res.,* **111,** B11307, doi: 10.1029/2006JB004311.

Forbriger, T., 2007. Reducing magnetic field induced noise in broad-band seismic recordings, *Geophys. J. Int.,* **169,** 240–258.

Forbriger, T., 2012. Information sheet 5.4: recommendations for seismometer deployment and shielding, In: *New Manual of Seismological Observatory Practice 2 (NMSOP2),* ed. Bormann, P., 2nd edn. Potsdam, Germany, doi:10.2312/GFZ.NMSOP-2-IS-5.4.

Forbriger, T., Widmer-Schnidrig, R., Wielandt, E., Hayman, M. & Ackerley, N., 2010. Magnetic field background variations can limit the resolution of seismic broad-band sensors, *Geophys. J. Int.,* **183,** 303–312.

Forbriger, T., Zürn, W. & Widmer-Schnidrig, R., 2021. Challenges and perspectives for lowering the vertical long period detection level, *Seismol. Res. Lett.,* **92**(4), 2498–-2512.

Gebauer, A., Steffen, H., Kroner, C. & Jahr, T., 2010. Finite element modelling of atmosphere loading effects on strain, tilt and displacement at multi-sensor stations, *Geophys. J. Int.,* **181,** 1593–1612.

Harrison, J.C., 1976. Cavity and topographic effects in tilt and strain measurement, *J. geophys. Res.,* **81,** 319–328.

Jackson, B.V. & Slichter, L.B., 1974. The residual daily tides at the South Pole, *J. geophys. Res.,* **79,** 1711–1715.

King, G.C.P. & Bilham, R.G., 1973. Tidal tilt measurement in Europe, *Nature,* **243,** 74–75.

King, G.C.P., Zürn, W., Evans, R. & Emter, D., 1976. Site corrections for long-period seismometers, tilt- and strainmeters, *Geophys. J. R. astr. Soc.,* **44,** 405–411.

Kurrle, D. & Widmer-Schnidrig, R., 2006. Spatiotemporal features of the Earth's background oscillations observed in central Europe, *Geophys. Res. Lett.,* **29,** L24304, doi: 10.1029/2006GL028429.

Kurrle, D. & Widmer-Schnidrig, R., 2008. The horizontal hum of the Earth: a global background of spheroidal and toroidal modes, *Geophys. Res. Lett.,* **33,** L06304, doi: 10.1029/2007GL033125.

Lambotte, S., Rivera, L. & Hinderer, J., 2006. Vertical and horizontal seismometric observations of tides, *J. Geodyn.,* **41,** 39–58.

Möckli, A., 1988. Versuche zur Luftdruckabschirmung langperiodischer Seismometer, p. 93, Diploma thesis, Geophysics, ETH Zürich, Switzerland.

Müller, T. & Zürn, W., 1983. Observation of gravity changes during the passage of cold fronts, *J. geophys.,* **53**(3), 155–162.

Park, J., Amoruso, A., Crescentini, L. & Boschi, E., 2008. Long-period toroidal earth free oscillations from the great Sumatra-Andaman earthquake observed by paired laser extensometers in Gran Sasso, Italy, *Geophys. J. Int.,* **173,** 887–905.

Ringler, A.T., Wilson, D.C., Zürn, W. & Anthony, R.E., 2019. Rayleigh wave ellipticity measurement uncertainty across the IRIS/USGS and New China Digital Seismograph Networks, *Geophys. J. Int.,* **217,** 219–237. 10.1093/gji/ggy527.

Rosat, S. & Hinderer, J., 2011. Noise levels of superconducting gravimeters: updated comparison and time stability, *Bull. seism. Soc. Am.,* **101**(3), 1233–1241.

Scripps Institution of Oceanography, 1986. IRIS/IDA Seismic Network, International Federation of Digital Seismograph Networks, Dataset/Seismic Network, doi:10.7914/SN/II.

Sorrells, G.G., 1971. A preliminary investigation into the relationship between long-period seismic noise and local fluctuations in the atmospheric pressure field, *Geophys. J. R. astr. Soc.,* **26,** 71–82.

Steffen, H., 2005. The importance of instrument location on barometric pressure-induced noise, *Bull. Inf. Marées Terrestres,* **141,** 11293–11302.

Steffen, H., Kuhlmann, S., Jahr, T. & Kroner, C., 2006. Numerical modelling of the barometric pressure-induced noise in horizontal components for the observatories Moxa and Schiltach, *J. Geodyn.,* **41,** 242–252.

Wielandt, E., 2002. Seismometry, Chapter 18 in: *Int. Handbook on Earthquake and Engineering Seismology, Part A,* pp. 283–304, eds Lee, W.H.K., Kanamori, H., Jennings, P.C. & Kisslinger, C., Academic Press, Amsterdam.

Wielandt, E. & Streckeisen, G., 1982. The leaf-spring seismometer: design and performance, *Bull. seism. Soc. Am.,* **72A,** 2349–2368.

Zürn, W., 2014. Listening to the Earth–the Schiltach Observatory (BFO), In *50 Years Geophysical Institute Karlsruhe, 1964-2014 - Expectations and Surprises,* pp. 285–309, ed Prodehl, C., Geophys. Inst. Karlsruhe Institute of Technology (KIT), Karlsruhe, Germany, doi:10.5445/IR/1000043755.

Zürn, W., Exß, J., Steffen, H., Kroner, C., Jahr, T. & Westerhaus, M., 2007. On reduction of long-period horizontal seismic noise using local barometric pressure, *Geophys. J. Int.,* **171,** 780–796.

Zürn, W., Ferreira, A.M.G., Widmer-Schnidrig, R., Lentas, K., Rivera, L. & Clévédé, E., 2015. High-quality lowest-frequency normal mode strain observations at the Black Forest Observatory (SW-Germany) and comparison with horizontal broad-band seismometer data and synthetics, *Geophys. J. Int.,* **203**(3), 1786–1803.

Zürn, W., Laske, G., Widmer-Schnidrig, R. & Gilbert, F., 2000. Observation of Coriolis coupled modes below 1 mHz, *Geophys. J. Int.,* **143,** 113–118.

Zürn, W. & Timmen, L., 2018. Krustendeformation und Schwereänderungen im seismischen Eigenschwingungsband durch Vorgänge in der Atmosphäre - ein Fallbeispiel, *Allg. Verm. Nachr.,* **5,** 127–132.

Zürn, W. & Widmer, R., 1995. On noise reduction in vertical seismic records below 2 mHz, *Geophys. Res. Lett.,* **22,** 3537–3540.

Zürn, W. & Wielandt, E., 2007. On the minimum of vertical seismic noise near 3 mHz, *Geophys. J. Int.,* **168,** 647–658.